

1 **Directly Measured Heating Rates of a Tropical Subvisible Cirrus Cloud**

2

3 **Anthony Bucholtz^{1*}, Dennis L. Hlavka², Matthew J. McGill³, K. Sebastian Schmidt⁴,**

4 **Peter Pilewski⁴, Sean M. Davis⁵, Elizabeth A. Reid¹, and Annette L. Walker¹**

5

6 ¹Naval Research Laboratory, Monterey, CA

7 ²Science Systems and Applications, NASA Goddard Space Flight Center, Greenbelt, MD

8 ³NASA Goddard Space Flight Center, Greenbelt, MD

9 ⁴University of Colorado, Boulder, CO

10 ⁵NOAA Earth System Research Laboratory, Boulder, CO

11

12

13

14

15

16

17

18

19

20 *Corresponding Author: Anthony Bucholtz, Marine Meteorology Division, Naval
21 Research Laboratory, 7 Grace Hopper Ave., Stop 2, Monterey, CA 93943-5502 Tel: 831-
22 656-5024, Fax: 831-656-4769, Email: anthony.bucholtz@nrlmry.navy.mil

23 **Abstract**

24 We present the first direct measurements of the infrared and solar heating rates of a
25 tropical subvisible cirrus (SVC) cloud sampled off the east coast of Nicaragua on 25 July
26 2007 by the NASA ER-2 aircraft during the Tropical Composition, Cloud and Climate
27 Coupling Experiment (TC4). On this day a persistent thin cirrus layer, with mostly clear
28 skies underneath, was detected in real-time by the cloud lidar on the ER-2 and the aircraft
29 was directed to profile down through the SVC. Measurements of the net broadband
30 infrared and solar irradiance above, below, and through the SVC are used to determine
31 the infrared and solar heating rates of the cloud. The lidar measurements show that the
32 variable SVC layer was located between ~13-15 km. Its midvisible optical depth varied
33 from 0.01-0.1, but was mostly in the 0.02-0.05 range, and its depolarization ratio was
34 approximately 0.4, indicative of ice clouds. From the divergence of the measured net
35 irradiances the infrared heating rate of the SVC was determined to be $\sim 2.50\text{-}3.24 \text{ K day}^{-1}$
36 and the solar heating rate was found to be negligible. These values are consistent with
37 previous indirect observations of other SVC and with model-generated heating rates of
38 SVC with similar optical depths. This study illustrates the utility and potential of the
39 profiling sampling-strategy employed here. A more fully instrumented high altitude
40 aircraft that also included in situ cloud and aerosol probes would provide a
41 comprehensive dataset for characterizing both the radiative and microphysical properties
42 of these ubiquitous tropical clouds.

43

44 **1. Introduction**

45 Subvisible cirrus (SVC) are high altitude, optically thin ice clouds that are very
46 common in the tropics. They are called subvisible because they are difficult to see
47 visually from below or above and only become apparent when viewed edge-on, as when
48 looking towards the horizon from an airplane. As a general rule of thumb it has been
49 estimated that a mid-visible cloud optical depth of approximately 0.03 is the minimum
50 threshold for visual observation of these clouds (Sassen and Cho, 1992).

51 The extent and prevalence of subvisible cirrus was first detected by ground based
52 lidar measurements in the western tropical Pacific at Kwajalein Atoll in the 1970s (Uthe
53 and Russel, 1976). Subsequent satellite (Prabhakara et al., 1993; Wang et al., 1996;
54 Winker and Trepte, 1998; Dessler et al., 2006; Mace et al., 2009), aircraft lidar
55 (McFarquhar et al., 2000; Pfister et al., 2001) and ground-based lidar (Comstock et al.,
56 2002) studies have confirmed the prevalence of SVC in the tropics and found that they
57 are present approximately 30-50% of the time depending on location. These studies have
58 also found that the SVC are located near the tropopause at altitudes of 14-17 km and are
59 typically less than a kilometer thick. They can be variable in space and time or they can
60 extend for hundreds of kilometers across the sky and last for several days. SVC have
61 been detected as a single isolated layer or as a layer above deep convection.

62 Since their discovery over thirty years ago there have only been a few direct aircraft
63 measurements of SVC, and these have been limited to measurements of the
64 microphysical properties of the clouds. Heymsfield (1986) performed the first in situ
65 measurements of SVC acquiring data on the habits and sizes of the ice crystals in the
66 cloud from a WB-57 aircraft over Kwajalein in 1973. Since then only a few in situ

67 aircraft microphysical measurement studies have occurred (Booker and Stickel, 1982;
68 Peter et al., 2003; Lawson et al., 2007). Recently, Davis et al. (2009, this issue) reported
69 on aircraft in situ and lidar measurements of the microphysical properties of subvisible
70 cirrus made from the NASA WB-57 aircraft during the TC4 field study near Costa Rica.

71 This lack of measurements has left many uncertainties about the radiative and
72 microphysical properties and effects of subvisible cirrus, and about their formation and
73 persistence mechanisms. However, because of the prevalence of SVC in the tropics,
74 several studies have suggested that these clouds may play an important role in the
75 radiative balance of the tropical upper troposphere and in stratosphere-troposphere
76 exchange by absorbing outgoing thermal infrared (IR) radiation and causing a subsequent
77 modification of the thermodynamic structure of the upper troposphere (Gage et al., 1991;
78 Jensen et al., 1996b; Rosenfield et al., 1998; Corti et al., 2006). This heating of the cloud
79 layer may also play a role in the persistence of the SVC by either warming the cloud and
80 causing it to dissipate in a matter of hours or by inducing a lifting of the cloud and
81 causing it to persist for days (Jensen et al. 1996a). Two recent modeling studies have
82 suggested that the IR heating of the SVC thermally forces a mesoscale circulation that
83 enables the cloud to maintain itself for up to 2 days (Durrán et al., 2009; Dinh et al.,
84 2009).

85 To address these issues accurate estimates of the radiative heating rates of the SVC
86 are required. Several studies have estimated SVC heating rates of a few K per day
87 (Jensen et al., 1996a; McFarquhar et al., 2000; Comstock et al., 2002). In general, these
88 studies estimated the heating rates with a radiative transfer model using as input the
89 microphysical data from the limited set of in situ aircraft measurements, and optical depth

90 and cloud boundary information from lidar measurements. Until now there has not been
91 a direct measurement of the heating rates of subvisible cirrus to validate these estimates.

92 Here we present the first direct measurements of the infrared and solar heating rates
93 of a tropical subvisible cirrus cloud sampled off the east coast of Nicaragua on 25 July
94 2007 by the NASA ER-2 aircraft during TC4. For almost the entire flight on this day the
95 downlooking cloud lidar on the ER-2 detected a persistent subvisible cirrus layer near the
96 bottom of the tropopause, with mostly clear skies underneath. Fortunately, the ER-2 had
97 a satellite downlink capability during TC4 and the cloud lidar data showing the presence,
98 altitude and thickness of the SVC below the aircraft was available to view in real time on
99 the ground enabling mission scientists to vector the ER-2 pilot to the proper altitudes and
100 coordinates to profile through this cirrus layer. Measurements from this flight of the net
101 broadband infrared and solar irradiance above, below, and through the SVC are used to
102 directly determine the infrared and solar heating rates of the cloud. In section 2 we
103 describe the instruments on the ER-2 that were used in this study, specifically, the
104 Broadband IR Radiometers (BBIR), the Solar Spectral Flux Radiometer (SSFR), and the
105 Cloud Physics Lidar (CPL). In section 3 we present the meteorological conditions on this
106 day and the morphological and optical properties of the SVC measured by the lidar. In
107 section 4 we illustrate the aircraft profiling strategy used to sample the SVC layer. In
108 section 5 we present the results of our measurements of the IR and solar heating rates of
109 the subvisible cirrus. In section 6 we compare our measurements to model generated
110 values and in section 7 we summarize our results and make suggestions for future aircraft
111 measurements of SVC.

112

113 **2. Instrument Description**

114 **2.1. Broadband Infrared Radiometers (BBIR)**

115 The BBIRs are Kipp & Zonen CG-4 pyrgeometers (Kipp & Zonen, 2003) that have
116 been modified to make them better suited for use on an aircraft (Bucholtz and Jonsson,
117 2009). They have a hemispheric field-of-view and a wavelength bandpass of 4.5-42 μm .
118 For TC4 identical BBIRs were mounted on the top and bottom of the ER-2 fuselage to
119 measure the downwelling and upwelling IR irradiance, respectively.

120 The modifications made to these commercially available radiometers include a new
121 back housing that retains the front end optics and electronics of the original instrument
122 but allows an amplifier to be mounted directly below the sensor. The signal is then
123 amplified from the milli-Volt range to the 0-10 Volt range and the instrument is run in
124 current loop mode, a well established technique for minimizing the effects of noise in
125 long signal cables. This technique is especially effective in the electronically noisy
126 environment of a research aircraft. The new housing has the cable connector on the
127 bottom of the instrument for easier mounting onto the aircraft. It is hermetically sealed
128 and has a pop-up pressure relief valve that allows evacuation of air from inside the
129 instrument to prevent damage or data loss due to condensation or freezing inside the
130 instrument dome.

131 The Kipp & Zonen pyrgeometers have features that make them attractive for aircraft
132 use even before modification. The off-the-shelf CG-4s have a silicon dome that acts as a
133 solar blind filter and has an ellipse shape with a full 180° field-of-view with a good
134 cosine response. Due to the construction methods used, any solar radiation absorbed by
135 the window is effectively conducted away, allowing accurate measurements in full

136 sunlight and eliminating the need for any shading disk. In addition, excellent dome to
137 body thermal coupling eliminates the need for a dome thermistor, and the calculation of
138 the dome to body temperature offset that is required by other pyrgeometers (Kipp &
139 Zonen, 2003; Philipona et al., 1995).

140 The BBIRs were calibrated in-house both pre- and post-mission. The calibration
141 entailed having the BBIRs view a blackbody source whose temperature was varied. The
142 calibration constants were then derived from a fit of the known blackbody irradiance at
143 each temperature versus the raw BBIR signal (in Volts). The pre- and post-mission
144 calibrations agreed to within 5% for the downlooking radiometer and to within 2% for the
145 uplooking radiometer, showing the stability of the BBIRs over the course of TC4.

146 As an additional test, side-by-side comparisons were done of the up- and down-
147 looking BBIRs used on the ER-2. This test simply involved mounting the two BBIRs
148 outside right next to each other and comparing the IR irradiances measured by each under
149 varying sky conditions. This comparison is especially important for this study because in
150 the determination of SVC heating rates we use the net flux, or difference between the up-
151 and down-looking radiometer measurements. The relative error between the two
152 instruments is therefore more important than the absolute error of each. The side-by-side
153 comparison test showed that the two BBIRs agreed to within +/- 1.0%. Based on these
154 calibrations and tests the accuracy of the BBIRs is estimated to be 2-5% and the precision
155 is estimated to be 1-3%.

156

157 **2.2 Solar Spectral Flux Radiometer (SSFR)**

158 The SSFR (Pilewskie et al., 2003) consists of two spectroradiometers connected via
159 fiber optic cables to optical inlets containing a miniature integrating sphere for light
160 collection. An optical inlet was mounted on the top (zenith viewing) and bottom (nadir
161 viewing) of the NASA ER-2 fuselage for TC4 to measure the downwelling and upwelling
162 spectrally resolved solar irradiance, respectively. The wavelength range of the
163 instrument, 350 to 2150 nm, encompasses 90% of incident solar radiation. This
164 wavelength range is covered by using two spectrometers per optical inlet: a grating
165 spectrometer with a Silicon Charged Coupled Device (CCD) array for near-ultraviolet,
166 visible and very near-infrared (350-1000 nm, 8 nm spectral resolution) and a
167 spectrometer with an Indium-Gallium-Arsenide linear array detector for the shortwave
168 infrared (900-2200 nm, 12 nm resolution) wavelength range. The SSFR records a nadir
169 and zenith spectrum every second.

170 The spectrometers are calibrated in the laboratory with a National Institute of
171 Standards and Technology (NIST)-traceable blackbody (tungsten-halogen 1000W bulb).
172 The radiometric stability of the SSFR is carefully tracked during the course of a field
173 experiment with a portable field calibration unit with a highly stable power source and
174 200W lamps. The calibration held to the 1 to 2% level over the course of the TC4 field
175 mission. The radiometric calibration was adjusted for minor fluctuations measured by
176 the field calibration from flight to flight. The estimated uncertainties in the absolute
177 calibration of the instrument are 5%. The data were corrected for the angular response of
178 the light collectors and for changes in downward irradiance due to aircraft attitude. The
179 attitude correction was necessary because the light collector reference plane (SSFR

180 horizon) deviated from horizontal alignment due to changes in aircraft pitch, roll, and
181 heading. No active stabilization was available for this experiment.

182

183 **2.3. Cloud Physics Lidar (CPL)**

184 The CPL is a multi-wavelength backscatter lidar built for use on the high altitude ER-
185 2 aircraft and was first deployed in 2000 (McGill et al., 2002; 2003). It was mounted in a
186 wing pod on the ER-2 for TC4 and looked downward. The CPL utilizes a high repetition
187 rate, low pulse energy transmitter and photon-counting detectors. It is designed
188 specifically for three-wavelength operation (355, 532, and 1064 nm, with depolarization
189 at 1064 nm) and maximum receiver efficiency. An off-axis parabola is used for the
190 telescope, allowing 100% of the laser energy to reach the atmosphere. The CPL is
191 designed with a nominal 100 microradian field of view to minimize the effects of
192 multiple scattering. CPL data products are typically provided at 30 m vertical resolution
193 and 1 second horizontal resolution (~200 m at the nominal ER-2 speed of 200 m/s).
194 Complete instrument details can be found in McGill et al. (2002).

195 The CPL fundamentally measures the total (aerosol plus Rayleigh) attenuated
196 backscatter as a function of altitude at each wavelength. Considerable data processing is
197 required to separate backscatter from clouds and aerosol and backscatter from Rayleigh.
198 However, for transmissive cloud/aerosol layers, using optical depth measurements
199 determined from attenuation of Rayleigh and aerosol scattering, and using the integrated
200 backscatter, the extinction-to-backscatter parameter (S-ratio) can be directly derived.
201 This permits unambiguous analysis of layer optical depth since only the lidar data is
202 required; there is no need to use other instrumentation nor is there need for assumptions

203 of aerosol climatology. Using the derived extinction-to-backscatter ratio, the internal
204 cloud extinction profile can then be obtained. This approach to directly solving the lidar
205 equation without assumption is a standard analysis approach for backscatter lidar and
206 more complete detail can be found in McGill et al. (2003).

207

208 **2.4. ER-2 Satellite Downlink (REVEAL):**

209 The TC4 mission provided the first opportunity for real time flight planning and aircraft
210 coordination. The NASA-developed Research Environment for Vehicle Embedded
211 Analysis on Linux (REVEAL) system

212 www.nasa.gov/centers/dryden/research/ESCD/OTH/Tools_Technologies/reveal.html

213 was installed on all three of the NASA aircraft participating in TC4 (i.e. the ER-2, WB-
214 57, and DC-8 aircraft). The REVEAL system permits real time reporting of the aircraft
215 location and, more importantly, provides a means for real time downlinking of data from
216 the aircraft instruments. The CPL onboard the ER-2 aircraft was one of the first
217 instruments to utilize this new capability. Although bandwidth limitations prohibited
218 downlinking of all CPL data, the CPL profiles were temporally subsampled at ~10
219 second intervals and sent to the TC4 mission operations center. Real time interpretation
220 of the CPL profiles permitted identification of subvisible cirrus layers and the aircraft
221 could then be vectored to the correct latitude, longitude and altitude to sample the SVC.

222

223 **3. Overview of 25 July 2007 ER-2 Subvisible Cirrus Case Study**

224 Figure 1 shows the entire flight track of the ER-2 on 25 July 2007 overlaid on the
225 GOES Visible image from 16:28 UTC (about midway into the flight). The altitude

226 profile of the ER-2 is shown in the inset of the figure. For TC4 the ER-2 was based out
227 of the Juan Santamaria Airport near San Jose, Costa Rica. On this day the ER-2 was the
228 only TC4 aircraft flying. Figure 1 shows that, for the most part, the ER-2 flew over the
229 apparent clear sky areas in the region avoiding the larger convective cells off the east
230 coast of Costa Rica (except on take-off and landing), and the smaller convective cell to
231 the North off the east coast of Honduras.

232 To put the radiometric and lidar measurements into context Figure 2 shows altitude
233 profiles of the temperature, wind direction, and wind speed as measured by the ER-2 on
234 its initial climb out over the Caribbean (red lines) and by balloonsondes launched from
235 Alajuela, Costa Rica before (blue lines) and near the end (green line) of the flight (Selkirk
236 et al. 2009; Vömel et al, 2007). The balloonsonde at 17:05 UTC did not measure winds.
237 Figure 2a shows the bottom of the tropopause was at ~15 km with a small inversion
238 between 15-16 km. That all three profiles show this same temperature structure indicates
239 the location of the tropopause and the inversion at 15-16 km were consistent throughout
240 the flight. Figures 2b and 2c show the winds were mostly out of the east and were
241 stronger below the tropopause.

242 Figure 3 shows the CPL attenuated backscatter signal as measured from the ER-2 for
243 the entire flight on this day. A variable, but persistent thin cirrus layer located between
244 approximately 13-15 km is apparent for most of the flight even though the GOES visible
245 satellite image (Figure 1) seems to indicate mostly clear skies along the flight track. The
246 thin cirrus layer occurs just below the bottom of the tropopause as indicated in Figure 2a.
247 The lidar data also shows that except for near the convective cloud regions it was mostly
248 clear underneath this thin cirrus layer for the majority of the flight, with only scattered

249 low clouds below 4 km. The ER-2 pilot reported that he could not see this thin cirrus
250 layer, even when he profiled through it. It only became apparent to him when he looked
251 towards the horizon.

252 Figure 4 shows the midvisible (532 nm) optical depth and depolarization ratio (at
253 1064 nm) derived from the lidar data for a representative section of the thin cirrus layer.
254 The data is given for the flight segment (times: 16:20-16:39 UTC) that occurred right
255 after the ER-2 had completed the profile down through the cirrus, climbed back up to
256 altitude, and then reversed course, overflying the same flight track and locations of the
257 profile. The optical depths and depolarization ratios in Figure 4 are therefore
258 representative of the cirrus sampled during the profile. The optical depth of the cirrus
259 layer varies between approximately 0.01 - 0.1 but is mostly in the range of 0.02 - 0.05.
260 These values are near or below the estimated minimum threshold for visual observation
261 of the cloud. The measured depolarization ratio is approximately 0.4, indicative of ice
262 clouds.

263 The low optical depths of these thin ice clouds and their location near the bottom of
264 the tropopause, combined with the fact that they do not show up in the visible satellite
265 image and they were not seen by the ER-2 pilot, are all consistent with these clouds being
266 subvisible cirrus.

267

268 **4. ER-2 Subvisible Cirrus Sampling Strategy**

269 The ER-2 for TC4 was meant to serve as a remote sensing platform, or satellite
270 surrogate, typically flying at a high, constant altitude of approximately 20 km. However,
271 three factors came together in TC4 that provided an opportunity to directly measure the

272 radiative heating rates of the subvisible cirrus by having the ER-2 deviate from its
273 nominal flight pattern and profile down through the cirrus layer. First, the high altitude
274 of the SVC put them within reach of the ER-2. Second, as described in section 2.4, the
275 ER-2 was equipped with a real-time downlooking cloud lidar that gave mission scientists
276 on the ground the ability to direct the ER-2 to the proper coordinates and altitudes to
277 sample the SVC. Third, the broadband IR and spectral solar irradiance radiometers on
278 the ER-2 provided measurements of the net irradiances as a function of altitude from
279 which the heating rates could be determined.

280 Figure 5 shows an idealized schematic of the flight profile flown by the ER-2 to
281 sample the subvisible cirrus layer. On the initial northbound heading in the Caribbean
282 (see Figure 1) the presence, altitude and thickness of the cirrus was detected in real-time
283 by the cloud lidar (see Figure 3). At the very north end of that leg the ER-2 began to pass
284 over a convective system off the east coast of Honduras. Therefore, the ER-2 was
285 directed to reverse course, and once south of the convection, was given the altitudes to
286 descend to in order to sample the previously seen SVC. As shown in Figure 5, the flight
287 pattern consisted of a level leg above and below the cloud, and a descent and ascent
288 through the cloud. The ER-2 began its initial descent from 20 km at approximately 15:25
289 UTC and eventually returned to its nominal altitude at approximately 16:30 UTC, so the
290 complete "dip" maneuver into the SVC took about 65 minutes. The flight times of each
291 leg are given in Figure 5.

292

293 **5. Measured Subvisible Cirrus Heating Rates**

294 The heating or cooling rate for a given layer in the atmosphere is defined as (Liou,
295 1980):

$$296 \quad \left(\frac{\partial T}{\partial t} \right) = 86400 \times \frac{g}{c_p} \frac{\nabla F}{\Delta p} \quad (1)$$

297 where T =temperature (degrees Kelvin), t =time (day), 86400=number of seconds per day,
298 g =gravitational acceleration (=980.616 cm sec⁻²), c_p =specific heat at constant pressure
299 (=1.004x10⁷ cm² sec⁻² K⁻¹), Δp is the difference in pressure between the lower and upper
300 altitude boundaries of the given layer, and ∇F is the difference between the net
301 irradiances at the lower and upper boundaries of the given altitude layer. The broadband
302 solar and IR net irradiances measured from the ER-2 as it profiled through the SVC layer
303 are used here to determine the heating rates of the cloud.

304 Figure 6 shows the net broadband solar irradiances measured by the SSFR instrument
305 on the ER-2 as it profiled through the SVC layer. The net broadband solar irradiance is
306 defined as the difference between the downwelling and upwelling solar irradiance at a
307 given altitude. While the SSFR is a spectral instrument we are interested here in
308 determining the complete solar heating rate of the SVC, therefore we have integrated the
309 SSFR signal over its complete wavelength range in order to get broadband solar
310 irradiances. The net solar irradiance measurements shown in Figure 6 have been
311 normalized to a common solar zenith angle of 24.162° to account for the change in
312 downwelling solar irradiance as the sun rose in the sky during this portion of the flight.
313 The data have also been corrected for the attitude (pitch, roll, and heading) of the aircraft.
314 The solar measurements during the 180° turn of the ER-2 on the below-cloud leg at
315 ~15:48 UTC have been filtered out. The dip in the measurements near 15:44 and 15:53
316 correspond to a low level cloud of limited extent.

317 Ignoring these dips it can be seen that there is no significant change in the net solar
318 irradiance as the ER-2 profiles through the SVC layer. The net solar irradiance
319 measurements for the above and below cloud legs are the same, and there is no change in
320 the net solar as the ER-2 descends or ascends through the cloud. In effect, the SVC is not
321 "seen" in the broadband solar irradiance data, indicating that there is no significant solar
322 radiative energy being deposited into or out of the SVC layer. The ∇F term in Eq. (1)
323 for this case is therefore near zero, and the solar heating rate for this SVC layer is zero or
324 negligible.

325 This is not the case for the IR measurements. Figure 7 shows the net broadband IR
326 irradiances measured by the BBIR instruments on the ER-2 as it profiled through the
327 SVC layer. The net broadband IR irradiance is defined as the difference between the
328 upwelling and downwelling IR irradiance at a given altitude. As we did for the solar
329 measurements, the IR measurements during the 180° turn of the ER-2 on the below-cloud
330 leg at about 15:48 UTC have been filtered out. The large dip in the net irradiance at
331 approximately 15:38 UTC and the smaller dip near 15:53 UTC correspond to lower level
332 clouds of limited extent below the SVC (also see the lidar image in Figure 3 for these
333 times).

334 Ignoring these dips in the data, it can be seen that the net IR irradiance at the level leg
335 just above the cirrus is less than the net IR irradiance at the level leg just below the cirrus,
336 and that the net IR irradiance increases approximately linearly with decreasing altitude
337 through the cloud. Since the primary source for thermal IR radiation in the atmosphere is
338 the Earth's surface (i.e. from below), the fact that the net IR irradiance above the cirrus is

339 smaller than the net IR irradiance below the cirrus indicates that IR radiative energy is
340 being deposited into the SVC layer. This IR energy will warm the layer.

341 Two methods were used to estimate the IR heating rate of the SVC layer. The first
342 method determined the heating rate from the difference in the net IR irradiance at the
343 level leg above and below the cirrus. For this case, the measured pressure and net IR
344 irradiance for each of the legs were averaged. For the above cloud leg the mean pressure
345 was 113.97 mb and the mean net IR irradiance was $275.16 \pm 3.33 \text{ W m}^{-2}$. For the below
346 cloud leg the mean pressure was 137.2 mb and the mean net IR irradiance was $282.03 \pm$
347 2.33 W m^{-2} . These values were put into Eq. (1) and using standard propagation of error
348 analysis (Bevington, 1969) the IR heating rate was found to be:

349
$$\text{IR Heating Rate (from level legs)} = 2.50 \pm 1.48 \text{ K day}^{-1}$$

350 The second method for estimating the IR heating rate used the net irradiance data
351 during the descent and ascent legs of the profile. At first glance, this would appear to be
352 a straightforward method. Simply use Eq. (1) to calculate the heating rate profile by
353 numerically differentiating the measured net IR irradiances with respect to pressure (i.e.
354 altitude) using a technique such as finite differencing. In practice this does not work
355 because the IR measurements are not ideal. They contain noise due to both
356 instrumentation issues and natural variability in the atmosphere (see Figure 7).and the
357 numerical differentiation of noisy data can lead to erroneous results (Chartrand, 2005).
358 Initial attempts to calculate the heating rate profile in this way led to wildly varying
359 results due to the rapidly fluctuating values of $\nabla F / \Delta p$ caused by the noise in the signal.
360 We therefore took a slightly different approach.

361 The net IR irradiances for the descent and ascent legs through the SVC were
362 combined and plotted as a function of pressure. The data from the dip in the
363 measurements due to the lower level cloud near 15:38 UTC was not included. Figure 8
364 shows that the measured net IR irradiances decrease linearly with decreasing pressure
365 (i.e. increasing altitudes). This indicates that the IR heating rate through the layer is
366 constant. The slope of the linear fit gives the change in the net IR irradiance per mb
367 pressure, that is, the slope of the fit gives

368
$$\frac{\nabla F}{\Delta p}$$

369 This was put into Eq. (1) and the IR heating rate was found to be:

370
$$\text{IR Heating Rate (from profile legs)} = 3.24 \pm 1.82 \text{ K day}^{-1}$$

371 The IR heating rates determined by the two methods are comparable and within the
372 error bars of each method. The first method that used the averaged net IR irradiances at
373 the legs below and above cloud probably gave a slightly lower heating rate because of the
374 dip in the measurements for part of the below cloud leg due to the lower level cloud that
375 the ER-2 passed over at 15:53 UTC. This consistency between the heating rates
376 determined by the two methods supports the validity of the values found.

377

378 **6. Comparison to Calculated Values**

379 The heating rates measured in this paper are consistent with previous model generated
380 values for subvisible cirrus of comparable optical depths. For example, Jensen et al.
381 (1996a) used a detailed cirrus cloud model and the in situ microphysical aircraft
382 measurements from Heymsfield (1986) to estimate heating rates of 1-3 K per day for
383 SVC with optical depths in the range of 0.01 to 0.03. McFarquhar et al. (2000) also used

384 the Heymsfield (1986) data, plus the in situ microphysical aircraft measurements of
385 Booker and Stickel (1982) and estimates of the SVC optical depth from the lidar on the
386 NASA ER-2 aircraft during the CEPEX field study in 1993 as input into the Fu and Liou
387 (1993) δ -four-stream radiative transfer code. Estimated heating rates of 1-2 K per day for
388 SVC with optical depths of approximately 0.01 were determined. Comstock et al. (2002)
389 used estimates of cloud optical depth and cloud base and top heights from surface lidar
390 measurements on Nauru Island as input into the Fu and Liou (1993) code and estimated
391 heating rates of approximately 3 K per day for a single SVC layer with an optical depth
392 of 0.022.

393 As a further test of the heating rates determined in this paper we computed the IR and
394 solar radiative heating rates for an SVC cloudy-sky case using the Rapid Radiative
395 Transfer Model (RRTM; Mlawer and Clough, 1997; Mlawer et al., 1997). RRTM uses a
396 correlated-k method for gaseous absorption, the Clough Kneizys Davies (CKD) 2.4 water
397 vapor continuum model (Clough et al., 1989), and cloud ice parameterizations based on
398 an effective size and water content (Fu et al., 1998; Fu, 1996). The key model input
399 parameters relevant to this study are the vertical profiles of atmospheric temperature,
400 ozone, water vapor, and cloud microphysical properties including the ice water path and a
401 generalized effective diameter for ice (D_{ge} , e.g., eqs. 3.11-3.12, Fu, 1996).

402 The vertical profiles of ozone, water vapor, and temperature are provided by the
403 Cryogenic Frostpoint Hygrometer (CFH; Vömel et al., 2007) and ECC ozonesonde
404 launched from the Juan Santamaria Airport in Alajuela, Costa Rica at 17 Z on 25 July
405 2007 (Selkirk et al., 2009). The water vapor measurements extend up to about 60 mb,
406 whereas the ozone and temperature measurements go to 10 mb. Above these levels, data

407 from the nearest overpass of the Microwave Limb Sounder (MLS) are used. For this
408 case, the solar zenith angle was 28° . For this RRTM model run the cloud optical depth,
409 τ , was set to 0.05. The cloud was distributed over a layer 0.5 km thick, and $r_e = 14 \mu\text{m}$
410 ($D_{ge} = 21 \mu\text{m}$), corresponding to the value found by in situ measurements during TC4
411 (Davis et al, 2009, this issue).

412 Figure 9 shows the solar and IR heating rates determined for this case. The calculated
413 solar heating rate in the cloud is 0.37 K day^{-1} and the calculated IR heating rate in the
414 SVC is 2.64 K day^{-1} . These values again are comparable to the negligible solar heating
415 rate and the $2.5\text{-}3.24 \text{ K day}^{-1}$ IR heating rate determined in this paper.

416

417 **7. Summary**

418 In this paper we determined the infrared and solar heating rates of a tropical
419 subvisible cirrus cloud through direct measurements of the net IR and solar irradiances
420 above, below, and through the cloud. The measurements were made from the NASA ER-
421 2 aircraft as it performed a rare descent profile down through an SVC layer off the east
422 coast of Nicaragua on 25 July 2007 during the TC4 field study. The ER-2 lidar
423 measurements showed that the variable SVC layer was located near the bottom of the
424 tropopause at approximately 13-15 km with mostly clear skies underneath. Its midvisible
425 optical depth varied from 0.01-0.1, but was mostly in the 0.02-0.05 range, and its
426 depolarization ratio was approximately 0.4, indicative of ice clouds. The solar heating
427 rate was found to be negligible, however, the infrared heating rate of the SVC was
428 determined to be approximately $2.50\text{-}3.24 \text{ K day}^{-1}$. These values were found to be

429 consistent with previous indirect observations of other SVC and with model-generated
430 heating rates of SVC with similar optical depths.

431 This direct measurement study therefore supports the current estimates that the
432 typical heating rate of the SVC is a few K per day with most of the heating occurring in
433 the IR. This study also illustrates the utility and potential of the profiling sampling-
434 strategy employed here and points to the need for more extensive sampling of subvisible
435 cirrus.

436 A high altitude aircraft that could make numerous profiles through multiple
437 subvisible cirrus equipped with solar and IR broadband and spectral radiometers, a real-
438 time cloud lidar, in situ cloud and aerosol probes, and state variable sensors would finally
439 provide a much needed comprehensive dataset for characterizing both the radiative and
440 microphysical properties of these ubiquitous tropical clouds.

441 **Acknowledgements**

442 We are grateful to Warren Gore and Tony Trias from NASA Ames Research Center
443 for their engineering and technical support during TC4, especially with the integration of
444 the BBIR instruments into the SSFR data acquisition system on the ER-2 aircraft. This
445 work was supported by the NASA Radiation Sciences Program under grant no.
446 NNH07AF56I (TC4).

447 **References**

- 448 Bucholtz, A., and H. Jonsson (2009), Modified Kipp & Zonen pyranometers and
449 pyrgeometers for use on atmospheric research aircraft, *J. Atmos. Oceanic Technol.*, in
450 preparation.
- 451 Booker, D. R., and P. G. Stickel (1982), High altitude tropical cirrus cloud observations,
452 *Conf. on Cloud Physics Preprint*, 215-217, Amer. Meteor. Soc., Chicago, IL.
- 453 Bevington, P. R. (1969), *Data Reduction and Error Analysis for the Physical Sciences*,
454 336 pp., McGraw-Hill Co., New York, New York.
- 455 Chartrand, R. (2005), Numerical differentiation of noisy, nonsmooth data, 9 pp., Los
456 Alamos National Laboratory, Los Alamos, NM.
- 457 Clough, S. A., et al. (1989), Line shape and the water vapor continuum, *Atmospheric*
458 *Research*, 23(3-4), 229-241.
- 459 Comstock, J. M., T. P. Ackerman, and G. G. Mace (2002), Ground-based lidar and radar
460 remote sensing of tropical cirrus clouds at Nauru island: Cloud statistics and radiative
461 impacts, *J. Geophys. Res.*, 107 (D23), 4714-4727, doi:10.1029/2002JD002203.
- 462 Corti, T., B. P. Luo, Q. Fu, H. Vomel, and T. Peter (2006), The impact of cirrus clouds on
463 tropical troposphere-to-stratosphere transport, *Atmos. Chem. and Phys.*, 6 (9), 2539-
464 2547.
- 465 Davis, S. M., D. Hlavka, E. Jensen, K. Rosenlof, S. Schmidt, S. Borrmann, W. Frey, P.
466 Lawson, H. Voemel, and T. P. Bui (2009), In situ and lidar observations of subvisible
467 cirrus clouds during TC4, *J. Geophys. Res.*, (submitted).

468 Dessler, A. E., S. P. Palm, W. D. Hart, and J. D. Spinhirne (2006), Tropopause-level thin
469 cirrus coverage revealed by ICESat/Geoscience Laser Altimeter System, *J. Geophys.*
470 *Res.*, *111*(D08), 203, doi:10.1029/2005JD006 586.

471 Dinh, T. P., D. R. Durran, and T. P. Ackerman (2009), The maintenance of tropical-
472 tropopause-layer cirrus, *J. Geophys. Res.*, submitted.

473 Durran, D. R., T. Dinh, M. Ammerman, and T. Ackerman (2009), The mesoscale
474 dynamics of thin tropical tropopause cirrus, *J. Atmos. Sci.*, in press.

475 Fu, Q., and K. N. Liou (1993), Parameterization of the radiative properties of cirrus
476 clouds, *J. Atmos. Sci.*, *50*, 2008-2025.

477 Fu, Q. A. (1996), An accurate parameterization of the solar radiative properties of cirrus
478 clouds for climate models, *J. of Climate*, *9*(9), 2058-2082.

479 Fu, Q., P. Yang, W. B. Sun (1998), An accurate parameterization of the infrared radiative
480 properties of cirrus clouds for climate models, *J. of Climate*, *11*(9), 2223-2237.

481 Gage, K. S., J. R. McAfee, D. A. Carter, W. L. Ecklund, A. C. Riddle, G. C. Reid, and B.
482 B. Balsley (1991), Long-Term Mean Vertical Motion over the Tropical Pacific:
483 Wind-Profiling Doppler Radar Measurements, *Science*, *254* (5039), 1771-1773.

484 Heymsfield, A. J. (1986), Ice Particles Observed in a Cirriform Cloud at -83°C and
485 Implications for Polar Stratospheric Clouds, *J. Atmos. Sci.*, *43*, no. 8, 851-855.

486 Jensen, E. J., O. B. Toon, H. B. Selkirk, J. D. Spinhirne, and M. R. Schoeberl (1996a),
487 On the formation and persistence of subvisible cirrus clouds near the tropical
488 tropopause, *J. Geophys. Res.*, *101*(D16), 21361-21375.

489 Jensen, E. J., O. B. Toon, L. Pfister, and H. B. Selkirk (1996b), Dehydration of the

490 upper troposphere and lower stratosphere by subvisible cirrus clouds near the tropical
491 tropopause, *Geophys. Res. Lett.*, 23(8), 825-828.

492 Kipp & Zonen (2003), *Instruction manual CG4 pyrgeometer*, 61 pp., Kipp & Zonen,
493 Delft, Netherlands.

494 Lawson, R. P., B. Pilon, B. Baker, Q. Mo, E. Jensen, L. Pfister, and P. Bui (2007),
495 Aircraft measurements of microphysical properties of subvisible cirrus in the tropical
496 tropopause layer, *Atmos. Chem. Phys. Discuss.*, 7, 6255-6292.

497 Liou, K.-N. (1980), *An Introduction to Atmospheric Radiation*, International Geophysics
498 Series, Vol. 26, 392 pp., Academic Press, Inc., San Diego, CA.

499 Mace, G. G., Q. Zhang, M. Vaughan, R. Marchand, G. Stephens, C. Trepte, and D.
500 Winker (2009), A description of hydrometeor layer occurrence statistics derived from
501 the first year of merged Cloudsat and CALIPSO data, *J. Geophys. Res.*, 114,
502 D00A26, doi: 10.1029/2007JD009755.

503 McFarquhar, G. M., A. J. Heymsfield, J. Spinhirne, and B. Hart (2000), Thin and
504 subvisual tropopause tropical cirrus: Observations and radiative impacts. *J. Atmos.*
505 *Sci.*, 57, no. 12, 1841-1853.

506 McGill, M., D. Hlavka, W. Hart, V. S. Scott, J. Spinhirne, and B. Schmid (2002), Cloud
507 Physics Lidar: instrument description and initial measurement results, *App. Opt.*, 41,
508 no. 18, 3725-3734.

509 McGill, M.J., D.L. Hlavka, W.D. Hart, E.J. Welton, and J.R. Campbell (2003), Airborne
510 lidar measurements of aerosol optical properties during SAFARI-2000, *J. Geophys.*
511 *Res.*, 108, doi: 10.1029/2002JD002370.

512 Mlawer, E., S. Taubman, P. Brown, M. Iacono, and S. Clough (1997), Radiative transfer
513 for inhomogeneous atmospheres: RRTM, a validated correlated-k model for the
514 longwave, *J. Geophys. Res.*, *102*(D14), 16663-16682.

515 Mlawer, E. J., and S. A. Clough (1997), On the extension of rapid radiative transfer
516 model to the shortwave region, *paper presented at 6th Atmospheric Radiation
517 Measurement (ARM) Science Team Meeting*, U.S. Department of Energy, CONF-
518 9603149.

519 Peter, T., B. P. Luo, M. Wirth, C. Kiemle, H. Flentje, V. A. Yushkov, V. Khattatov, V.
520 Rudakov, A. Thomas, S. Borrmann, G. Toci, P. Mazzinghi, J. Beuermann, C.
521 Schiller, F. Cairo, g. Di Donfrancesco, A. Adriani, C. M. Volk, J. Strom, K. Noone,
522 V. Mitev, R. A. MacKenzie, K. S. Carslaw, t. Trautmann, V. Santacesaria, and L.
523 Stefanutti (2003), Ultrathin tropical tropopause clouds (UTTCS): I. cloud morphology
524 and occurrence. *Atmos. Chem. Phys.*, *3*, 1083-1091.

525 Pfister, L., H. B. Selkirk, E. J. Jensen, M. R. Schoeberl, O. B. Toon, E. V. Browell, W. B.
526 Grant, B. Gary, M. J. Mahoney, T. V. Bui, and E. Hints (2001), Aircraft
527 observations of thin cirrus clouds near the tropical tropopause, *J. Geophys. Res.*,
528 *106*(D9), 9765-9786.

529 Philipona, R., C. Frohlich, and C. Betz (1995), Characterization of pyrgeometers and the
530 accuracy of atmospheric longwave radiation measurements, *Appl. Opt.*, *34*, 1598-
531 1605.

532 Pilewskie, P., J. Pommier, R. Bergstrom, W. Gore, S. Howard, M. Rabbette, B. Schmid,
533 P. V. Hobbs, and S. C. Tsay (2003), Solar spectral radiative forcing during the

534 Southern African Regional Science Initiative, *J. Geophys. Res.*, 108(D13), 8486,
535 doi:10.1029/2002JD002411.

536 Prabhakara, C., D. P. Kratz, J. -M. Yoo, G. Dalu, and A. Vernekar (1993), Optically Thin
537 Cirrus Clouds: Radiative Impact on the Warm Pool, *J. Quant. Spectrosc. Radiat.*
538 *Transfer*, 49, no. 5, 467-483.

539 Sassen, K., and B. S. Cho (1992), Subvisual-Thin Cirrus Lidar Dataset for Satellite
540 Verification and Climatological Research, *J. Appl. Meteor.*, 31, 1275-1285.

541 Selkirk, H. B., H. Vömel, J. Valverde, L. Pfister (2009), The detailed structure of the
542 tropical upper troposphere as revealed by balloonsonde observations of water vapor,
543 ozone, temperature and winds during the NASA TCSP and TC4 campaigns, *J.*
544 *Geophys. Res.*, (submitted).

545 Uthe, E. E., and P. B. Russell (1976), Lidar Observations of Tropical High-Altitude
546 Cirrus Clouds, *IAMAP Symposium on Radiation in the Atmosphere Preprints*, 74th,
547 Garmisch-Partenkirchen, Germany.

548 Vömel, H., D. E. David, and K. Smith (2007), Accuracy of tropospheric and stratospheric
549 water vapor measurements by the cryogenic frost point hygrometer: Instrumental
550 details and observations, *J. Geophys. Res.*, 112, D08305, doi:10.1029/2006JD007224.

551 Wang, P. H., P. Minnis, M. P. McCormick, G. S. Kent, and K. M. Skeens (1996), A 6-
552 year climatology of cloud occurrence frequency from Stratospheric Aerosol and Gas
553 Experiment II observations (1985-1990), *J. Geophys. Res.*, 101(D23), 29 407-29 429.

554 Winker, D. M. and C. R. Trepte (1998), Laminar cirrus observed near the tropical
555 tropopause by LITE. *Geophys. Res. Letts*, 25, no. 17, 3351-3354.

556 **Figure Captions:**

557 **Figure 1:** The ER-2 flight track on 25 July 2007 is shown overlaid on the GOES Vis
558 image from 16:28 UTC. The altitude profile of the ER-2 is given in the inset. The ER-2
559 was the sole TC4 aircraft flying on this day. (Image from NASA Langley TC4 Satellite
560 Page: <http://angler.larc.nasa.gov/tc4>).

561 **Figure 2:** Profiles of (a) temperature, (b) wind direction, and (c) wind speed as measured
562 by the ER-2 on its initial climb out over the Caribbean (red lines) and by balloonsondes
563 launched from Alajuela, Costa Rica before (blue lines) and near the end (green line) of
564 the flight. All three soundings in (a) show the bottom of the tropopause at approximately
565 15 km with a small inversion between 15-16 km. Winds were mostly out of the East (b)
566 and were stronger below the tropopause (c). (Selkirk et al. 2009; Vogel et al, 2007)

567 **Figure 3:** The CPL attenuated backscatter signal for the entire flight on 25July2007
568 showing a persistent thin cirrus layer between approximately 13-15 km altitude. The thin
569 cirrus layer occurs just below the bottom of the tropopause (see Fig. 2a). The ER-2
570 headings for the different flight segments over the Caribbean are also given
571 (N=northbound; S=southbound; W=westbound). The location of the ER-2 profile
572 through the cirrus is indicated, as well as the flight segment where the cloud optical
573 depths (OD) are given in Figure 4a.

574 **Figure 4:** The (a) optical depth and (b) depolarization ratio derived from the lidar data
575 for a representative section of the thin cirrus observed on 25July2007 between 16:20-
576 16:39 UTC (see Figure 3). The optical depth of the cirrus varies between approximately
577 0.01 to 0.1 but is mostly in the range of 0.02 to 0.05. The estimated threshold for visual

578 observation is 0.03. The depolarization ratio (b) for these clouds is approximately 0.4
579 indicative of ice clouds.

580 **Figure 5:** An idealized schematic of the flight profile flown by the ER-2 to sample the
581 subvisible cirrus layer. This flight pattern provided a level leg above and below the
582 cloud, and a descent and ascent through the cloud to measure the IR and solar broadband
583 net irradiances throughout the profile from which the heating rates were derived. The
584 UTC flight times of each leg are given. The altitudes given are approximate.

585 **Figure 6:** The net solar irradiances measured during the ER-2 profile through the
586 subvisible cirrus and the corresponding altitudes of each leg. The net solar irradiance
587 data for this time segment have been normalized to a solar zenith angle of 24.162° and
588 corrected for the attitude (pitch, roll, and heading) of the aircraft. The measurements
589 during the 180° turn of the ER-2 near 15:48 UTC have been filtered out. The dips in net
590 irradiance at approximately 15:43 and 15:53 correspond to lower level clouds below the
591 cirrus.

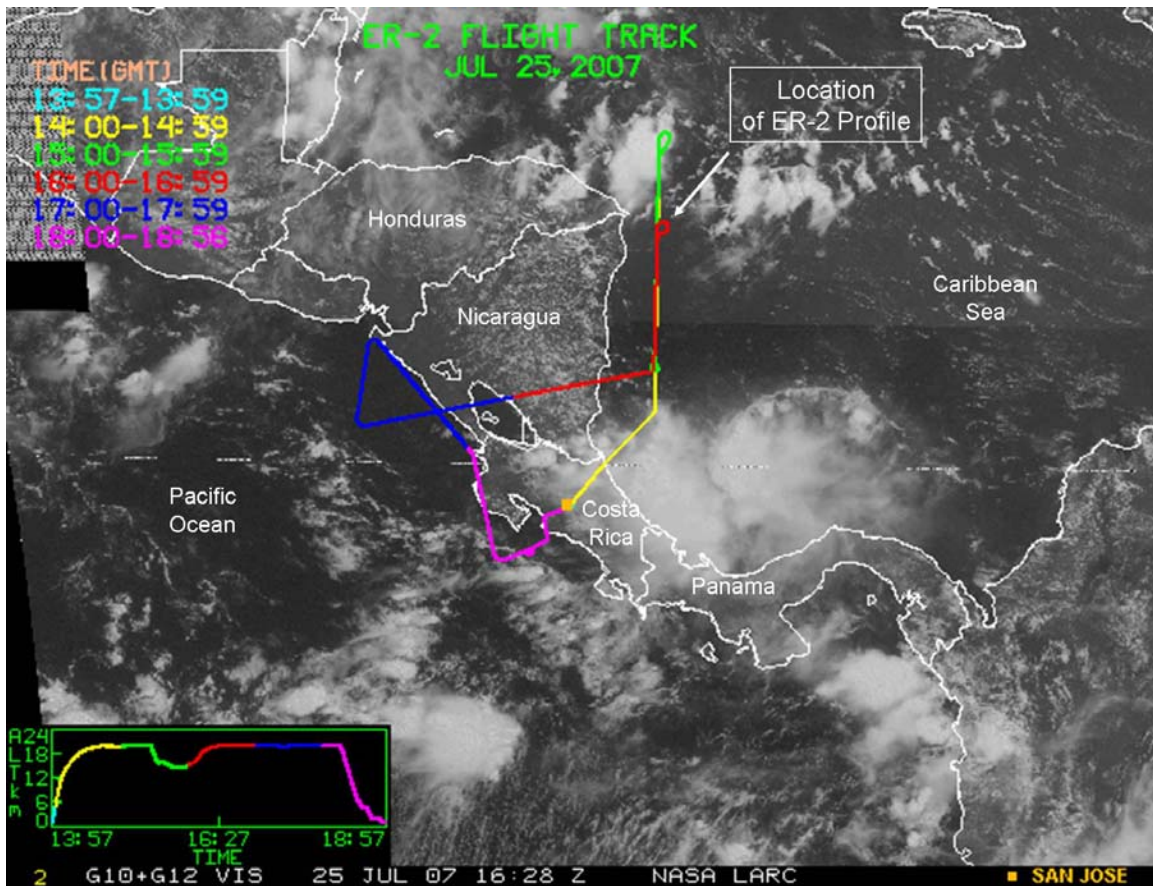
592 **Figure 7:** The net IR irradiances measured during the ER-2 profile through the
593 subvisible cirrus and the corresponding altitudes of each leg. Measurements during the
594 180° turn of the ER-2 near 15:48 UTC have been filtered out. The large dip in net flux at
595 approximately 15:38 and the smaller dip near 15:53 correspond to low level cloud below
596 the cirrus.

597 **Figure 8:** The net IR fluxes as a function of pressure for the descent and ascent of the
598 ER-2 through the thin cirrus layer are combined here. The linear decrease in the net flux
599 with altitude indicates a constant IR heating rate through the layer. The slope of the
600 linear fit (net flux per mb pressure) is used to derive the IR heating rate

601 **Figure 9:** Calculated IR and solar heating rates for an idealized subvisible cirrus cloud
602 using the RRTM radiative transfer code. Vertical profiles of atmospheric temperature,
603 ozone, and water vapor from balloonsondes launched from Costa Rica on 25 July 2007,
604 and cloud microphysical information from measurements of SVC during TC4 are used in
605 the calculations. The cloud was 0.5 km thick with an optical depth of 0.05.
606

607 **Figures:**

608



609

610

611

612

613 **Figure 1:** The ER-2 flight track on 25 July 2007 is shown overlaid on the GOES Vis

614 image from 16:28 UTC. The altitude profile of the ER-2 is given in the inset. The ER-2

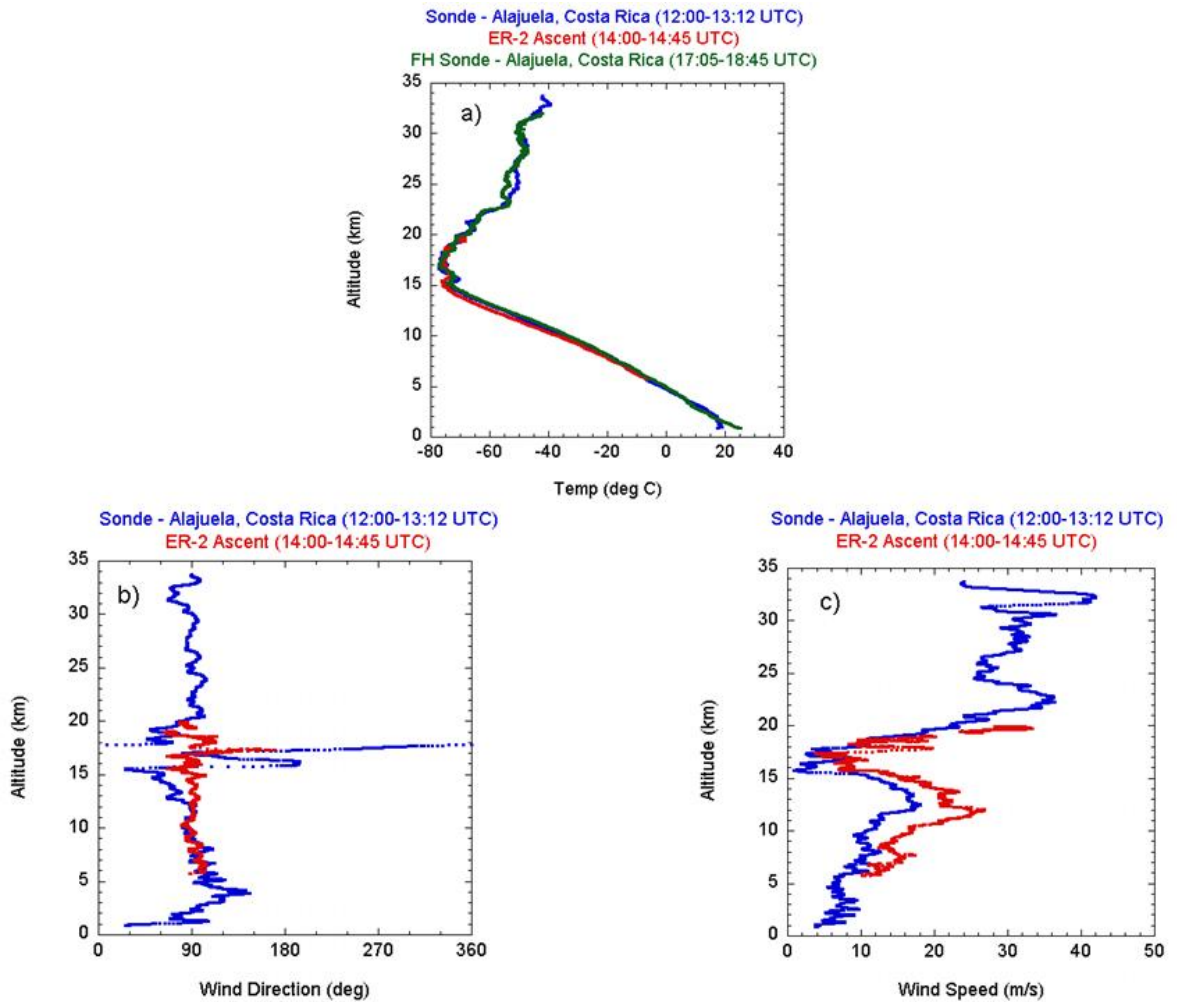
615 was the sole TC4 aircraft flying on this day. (Image from NASA Langley TC4 Satellite

616 Page: <http://angler.larc.nasa.gov/tc4>).

617

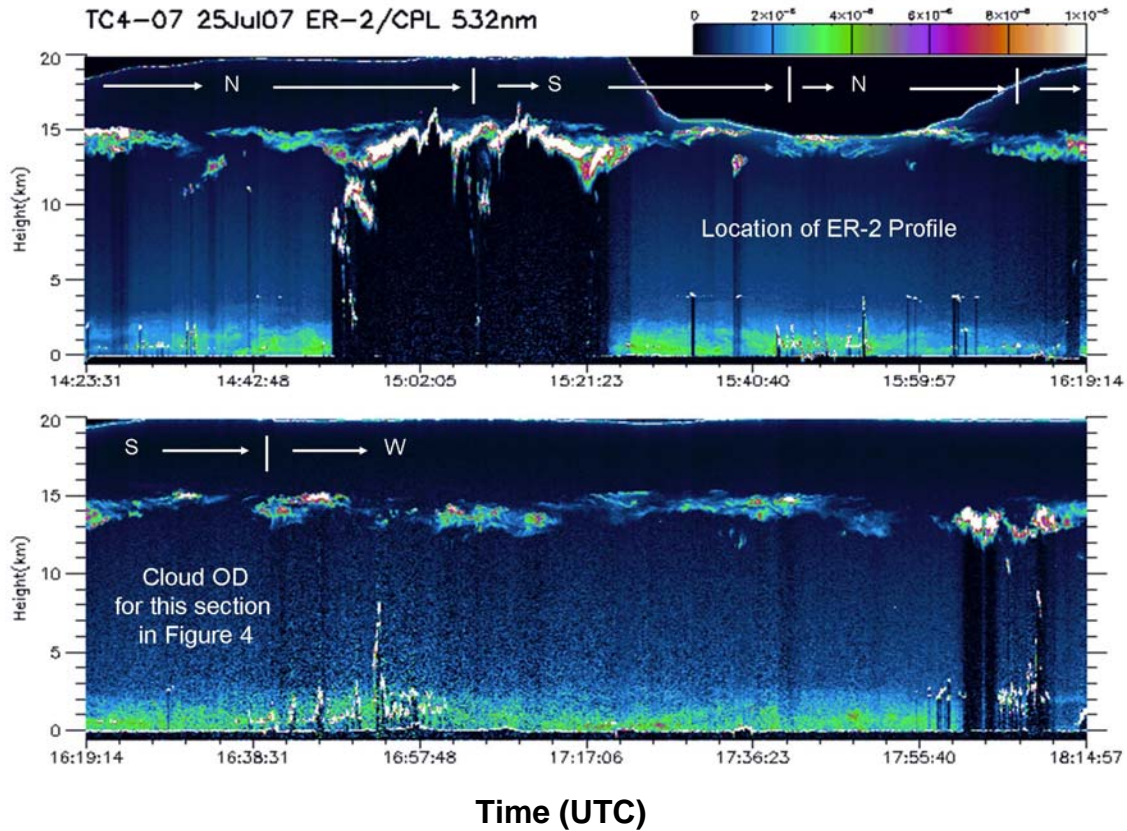
618

619
620



621
622
623
624
625
626
627
628
629
630
631

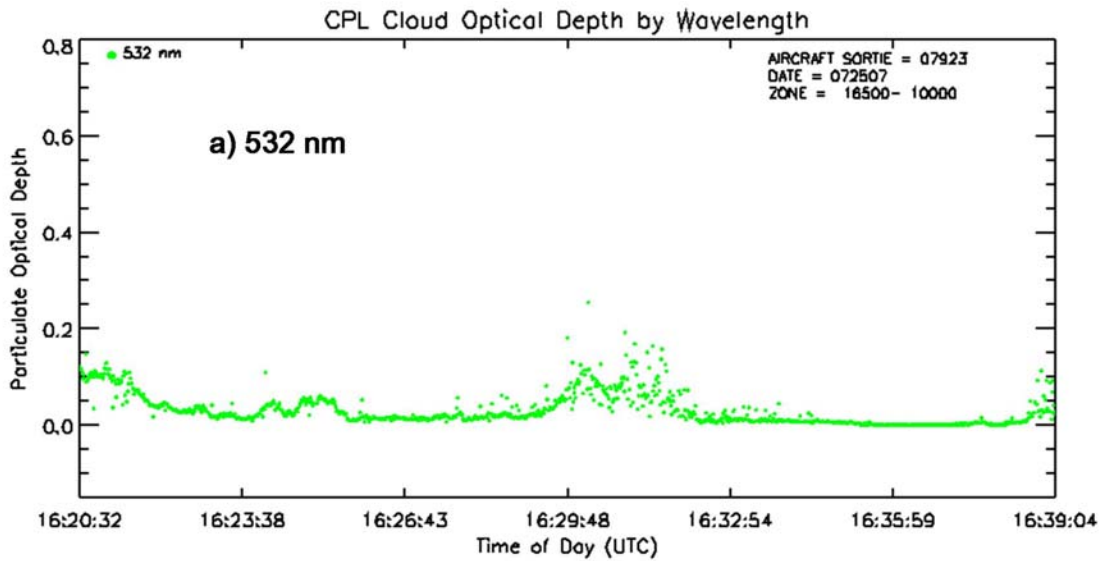
Figure 2: Profiles of (a) temperature, (b) wind direction, and (c) wind speed as measured by the ER-2 on its initial climb out over the Caribbean (red lines) and by balloonsondes launched from Alajuela, Costa Rica before (blue lines) and near the end (green line) of the flight. All three soundings in (a) show the bottom of the tropopause at approximately 15 km with a small inversion between 15-16 km. Winds were mostly out of the East (b) and were stronger below the tropopause (c). (Selkirk et al. 2009; Vogel et al, 2007)



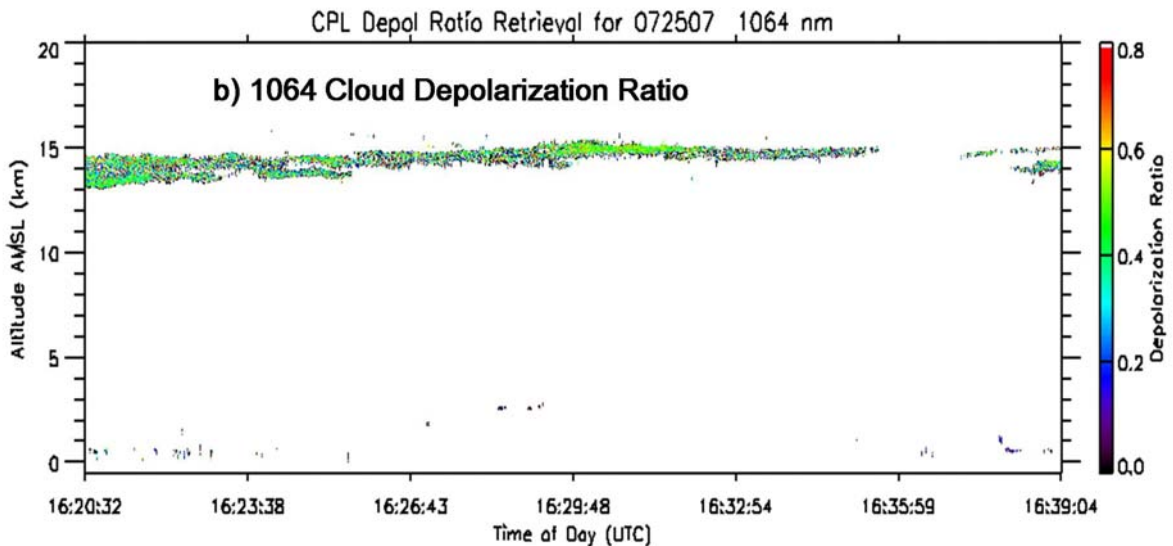
632
 633
 634
 635
 636
 637
 638
 639
 640
 641
 642
 643

Figure 3: The CPL attenuated backscatter signal for the entire flight on 25 July 2007 showing a persistent thin cirrus layer between approximately 13-15 km altitude. The thin cirrus layer occurs just below the bottom of the tropopause (see Fig. 2a). The ER-2 headings for the different flight segments over the Caribbean are also given (N=northbound; S=southbound; W=westbound). The location of the ER-2 profile through the cirrus is indicated, as well as the flight segment where the cloud optical depths (OD) are given in Figure 4a.

644



645



646

647

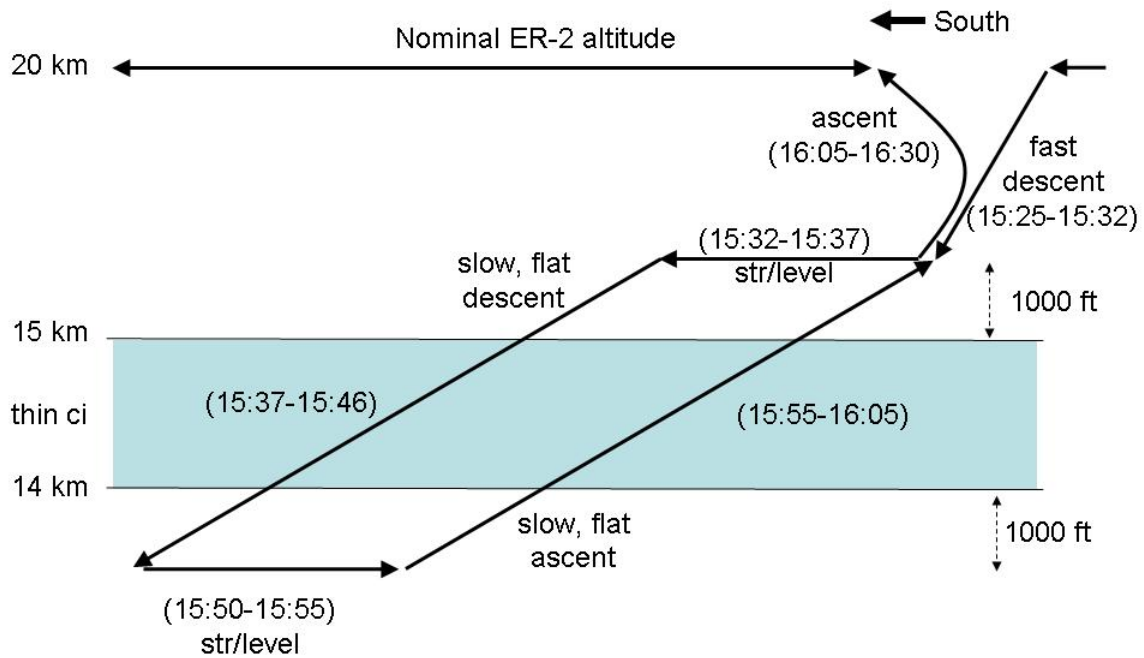
648 **Figure 4:** The (a) optical depth and (b) depolarization ratio derived from the lidar data
649 for a representative section of the thin cirrus observed on 25 July 2007 between 16:20-
650 16:39 UTC (see Figure 3). The optical depth of the cirrus varies between approximately
651 0.01 to 0.1 but is mostly in the range of 0.02 to 0.05. The estimated threshold for visual
652 observation is 0.03. The depolarization ratio (b) for these clouds is approximately 0.4
653 indicative of ice clouds.

654

655

656

657



658

659

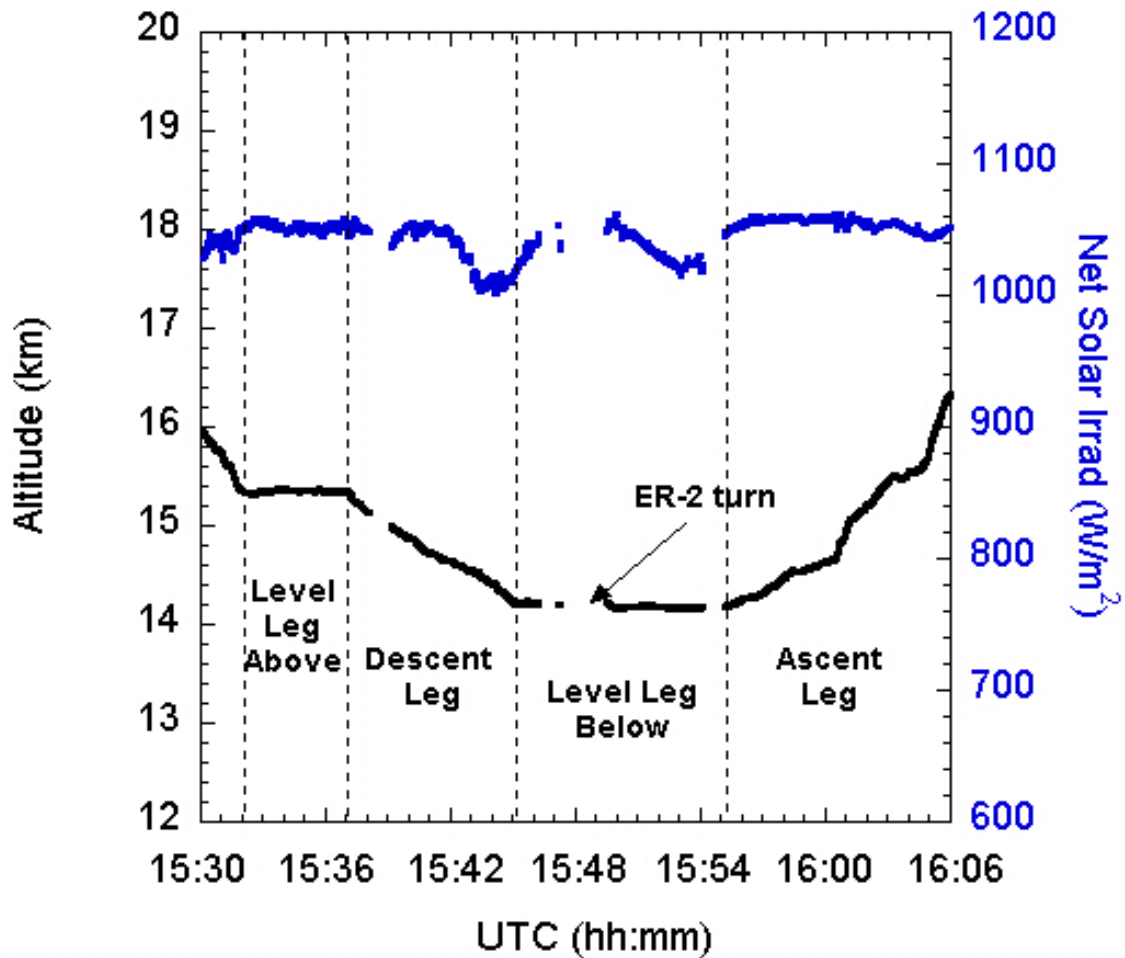
660 **Figure 5:** An idealized schematic of the flight profile flown by the ER-2 to sample the
661 subvisible cirrus layer. This flight pattern provided a level leg above and below the
662 cloud, and a descent and ascent through the cloud to measure the IR and solar broadband
663 net irradiances throughout the profile from which the heating rates were derived. The
664 UTC flight times of each leg are given. The altitudes given are approximate.

665

666

667

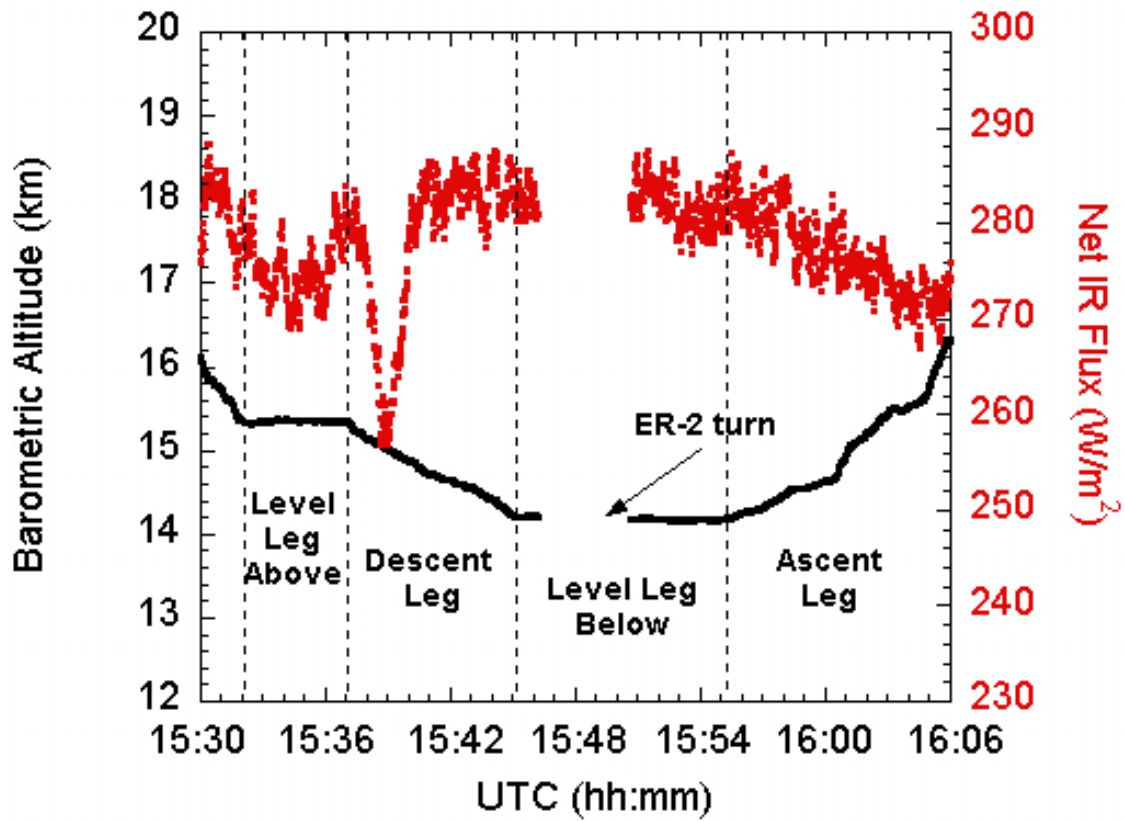
668
669
670
671



672
673
674
675
676
677
678
679
680
681
682

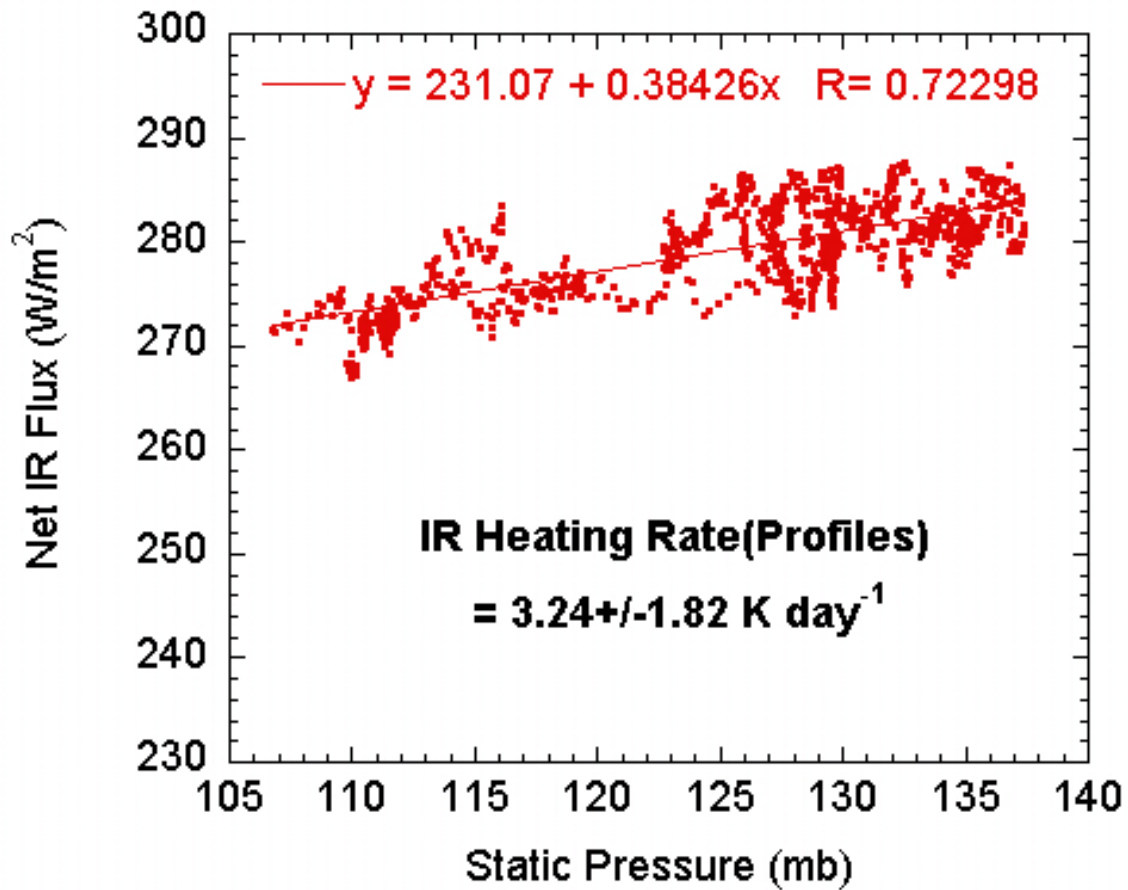
Figure 6: The net solar irradiances measured during the ER-2 profile through the subvisible cirrus and the corresponding altitudes of each leg. The net solar irradiance data for this time segment have been normalized to a solar zenith angle of 24.162° and corrected for the attitude (pitch, roll, and heading) of the aircraft. The measurements during the 180° turn of the ER-2 near 15:48 UTC have been filtered out. The dips in net irradiance at approximately 15:43 and 15:53 correspond to lower level clouds below the cirrus.

683
684
685
686



687
688
689
690
691
692
693
694
695

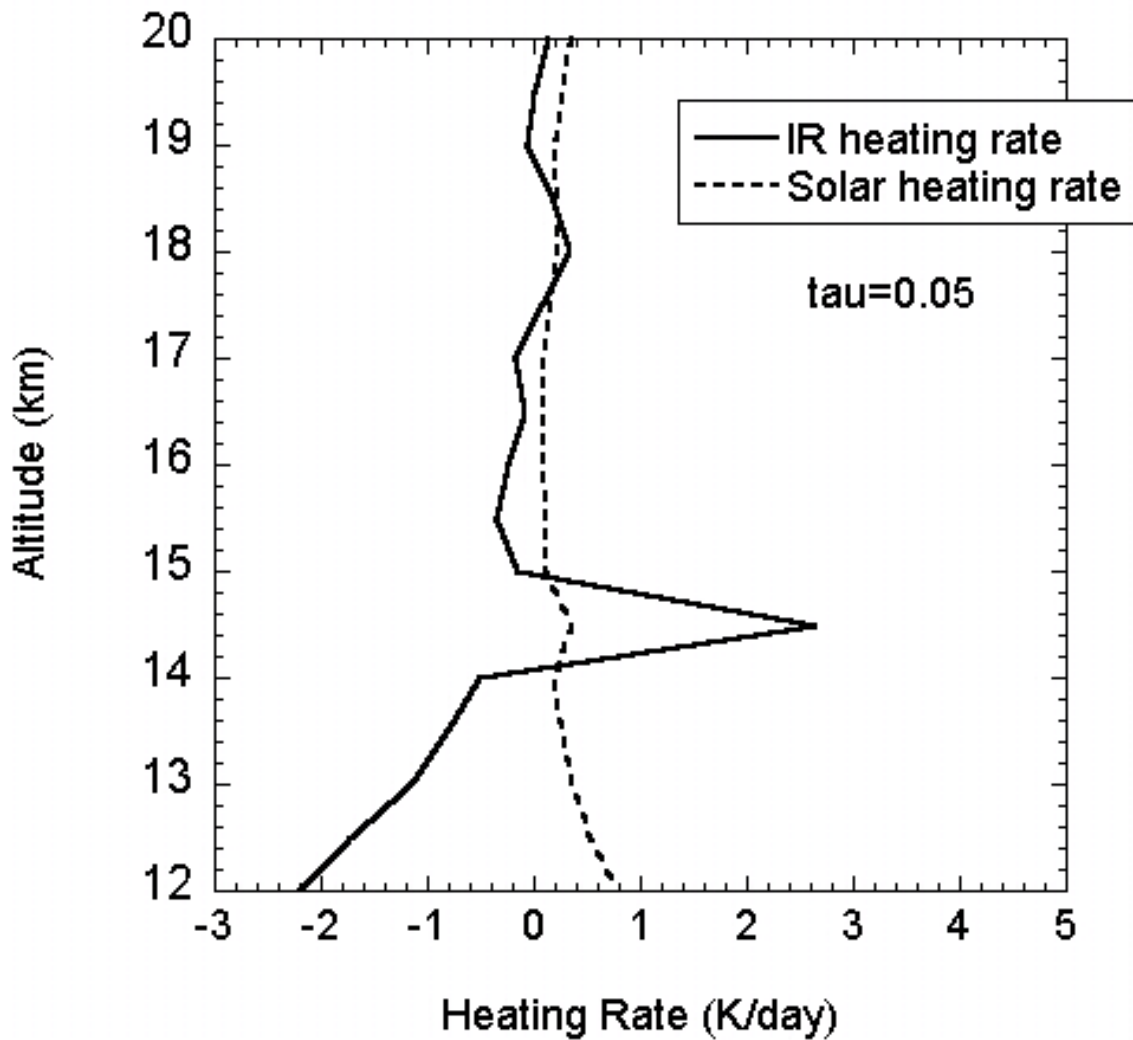
Figure 7: The net IR irradiances measured during the ER-2 profile through the subvisible cirrus and the corresponding altitudes of each leg. Measurements during the 180° turn of the ER-2 near 15:48 UTC have been filtered out. The large dip in net flux at approximately 15:38 and the smaller dip near 15:53 correspond to low level cloud below the cirrus.



697
 698
 699
 700
 701
 702
 703
 704

Figure 8: The net IR fluxes as a function of pressure for the descent and ascent of the ER-2 through the thin cirrus layer are combined here. The linear decrease in the net flux with altitude indicates a constant IR heating rate through the layer. The slope of the linear fit (net flux per mb pressure) is used to derive the IR heating rate

705
706
707



708
709
710
711
712
713
714
715
716
717
718
719

Figure 9: Calculated IR and solar heating rates for an idealized subvisible cirrus cloud using the RRTM radiative transfer code. Vertical profiles of atmospheric temperature, ozone, and water vapor from balloonsondes launched from Costa Rica on 25 July 2007, and cloud microphysical information from measurements of SVC during TC4 are used in the calculations. The cloud was 0.5 km thick with an optical depth of 0.05.